Ensemble and single-molecule dynamics of intraflagellar transport in C. elegans

Mijalkovic, J.

2018

document version
Publisher's PDF, also known as Version of record

3

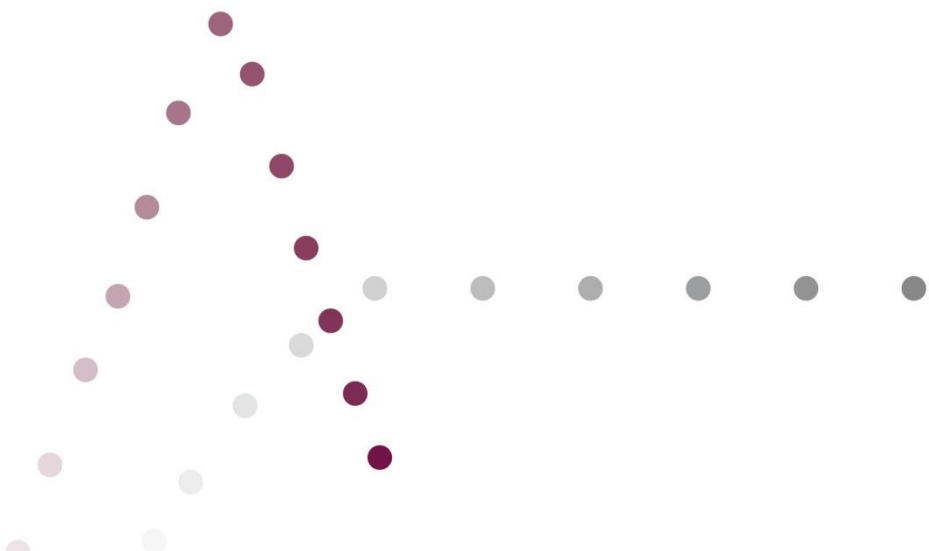

Single-molecule turnarounds of intraflagellar transport at the *C. elegans* ciliary tip

Jona Mijalkovic[*], Jaap van Krugten[*], Felix Oswald, Seyda Acar and Erwin J.G. Peterman

[*] these authors contributed equally

Submitted for publication

Abstract

Cilia are polar, microtubule-based cellular sensing hubs that rely on intraflagellar transport (IFT) for their development, maintenance and function. IFT trains, consisting of the IFT-A and IFT-B protein sub-complexes and cargo, are co-operatively driven from ciliary base to tip by kinesin-2 motors. At the tip, trains turn around and are transported back to the base by IFT dynein. The mechanism of this turnaround at the tip has remained elusive. Here, we employ single-molecule fluorescence microscopy of IFT components in the tips of phasmid cilia of living *C. elegans*. Analysis of the trajectories reveals distinct turnaround behavior of different IFT components: while the motor proteins and IFT-A particle sub-complexes mostly turn around immediately, IFT-B particle sub-complexes show substantial pauses, lasting several seconds (median 2.5 s). Our data show that IFT trains completely disassemble at the tip where IFT-B most likely undergoes modification, prior to train reassembly and retrograde transport. The single-molecule approach used here is a valuable tool to study how directional switches occur in microtubule-based transport processes.

3.1 Introduction

Primary cilia are microtubule-based, membrane-enveloped organelles projecting from the surface of most eukaryotic cells, with important roles in sensory perception and signaling [1]. They are built and maintained by the cooperative action of opposite-polarity motors, kinesin-2 and IFT dynein, in a process called intraflagellar transport (IFT) [2, 3]. Continuous IFT cycles, from base to tip (anterograde) and back from tip to base (retrograde), are necessary for ciliary functioning [4-6]. Defects in IFT are associated with human disorders called ciliopathies, including Bardet-Biedl syndrome and polycystic kidney disease [7, 8]. In IFT, groups of plus-end-directed kinesin-2 motors drive anterograde transport to the tip. At the ciliary tip, cargo is (un)loaded and IFT dynein engages to drive transport of IFT components and cargo back to the base. Despite recent progress in understanding IFT, little is known about IFT anterograde-to-retrograde turnaround at the tip.

IFT is a process involving many different proteins that move in large complexes called IFT trains. IFT trains are composed of several tens of mechanically coupled IFT-A and IFT-B sub-complexes that form a stable backbone to which the motors can dock on and off [9]. IFT trains are thought to be assembled at the base/transition zone region of the ciliary axoneme and subsequently move along the axonemal microtubules in the anterograde direction to deliver tubulin [10, 11], axonemal precursors [12], receptor ion channels [13], sensory receptors [14] and other cargoes to the distal tip. In *C. elegans* chemosensory cilia, anterograde IFT is carried out by two different motors of the kinesin-2 family: 'import motor' kinesin-II, which is restricted to the base, transition zone and the beginning of the proximal segment, and 'long-range' motor OSM-3, which takes over transport in the proximal segment and is the sole anterograde motor in the distal segment [9, 15, 16]. Only one type of retrograde motor, IFT dynein, is responsible for the return of turnover products to the ciliary base [17-20].

There is a growing body of evidence that IFT trains remodel at the ciliary tip. Recent electron microscopy (EM) studies in *C. reinhardtii* have shown that dynein-driven retrograde trains appear morphologically different from kinesin-driven anterograde trains [21, 22]. In *C. elegans* and *T. brucei*, it has been reported that the retrograde train frequency is higher than the anterograde frequency [23, 24]. Further insights have come from *C. reinhardtii* immunoprecipitation and *C. elegans* mutant studies. These studies showed that IFT-dynein light intermediate chain is bound to IFT-B during anterograde transport whereas it is bound to IFT-A during retrograde transport, suggesting that IFT trains undergo substantial remodeling at the ciliary tip [25, 26]. How remodeling and turnaround of IFT trains precisely occurs at the tip, however, remains poorly understood. Turnarounds of IFT-particle sub-complexes and IFT-dynein components have been reported at the ensemble level in different species [23, 27, 28]. A recent study investigating the dynamics of whole IFT trains in *Chlamydomonas*, demonstrated that IFT trains split apart at the tip [29]. Comprehensive, quantitative studies on the single-molecule level, however, have been lacking. We have shown before that a single-molecule view on this complex transport mechanism can reveal important insights in motor and train dynamics that are hidden in ensemble studies [9, 24].

Here, we use a similar single-molecule fluorescence microscopy approach to visualize the dynamics of IFT dynein, OSM-3, and the IFT-A and IFT-B particle sub-complexes at the tips of chemosensory cilia in living *C. elegans*. From sequences of the images we extract single-protein trajectories revealing direct turns and turns involving a pause close to the tip, in a turnaround region of approximately a micrometer in length. We show that IFT trains completely disassemble and reassemble at the tip, with IFT-B, in contrast to the other components, pausing for several seconds. This observation is consistent with a turnaround mechanism in which IFT-B or components of IFT-B undergo a modification that allows IFT trains to switch from anterograde to retrograde transport.

3.2 Results

In previous single-molecule studies of IFT in *C. elegans* phasmid cilia we noticed that it was difficult to obtain in-focus images of whole cilia [9, 24]. In most cases, the last ~micrometer, including the ciliary tip, was out-of-focus with respect to the rest of the cilium. To shed more light on this, we generated nematodes with labeled tubulin (TBB-4::EGFP, Supplementary Table 3.1) and used confocal fluorescence microscopy to obtain 3-dimensional images of cilia (Figure 3.1A, B). These images clearly show that the four phasmid cilia (PHAL, PHBL, PHAR and PHBR) are relatively straight, except for the last few micrometers, close to the tip, that bend out (Figure 3.1A, Supplementary Figure 3.1A). Some of the imaged worms (~5%) were oriented such that the PHA and PHB cilium pairs lie on top of each other (in the Z-direction, perpendicular to the plane of the image; Figure 3.1B, Supplementary Figure 3.1B). In these animals, the cilia are in a single Z-plane and can be brought into focus completely, including the ciliary tip. Below we will focus our measurements and analysis of IFT dynamics in the tip at the single-molecule level to animals in this particular orientation.

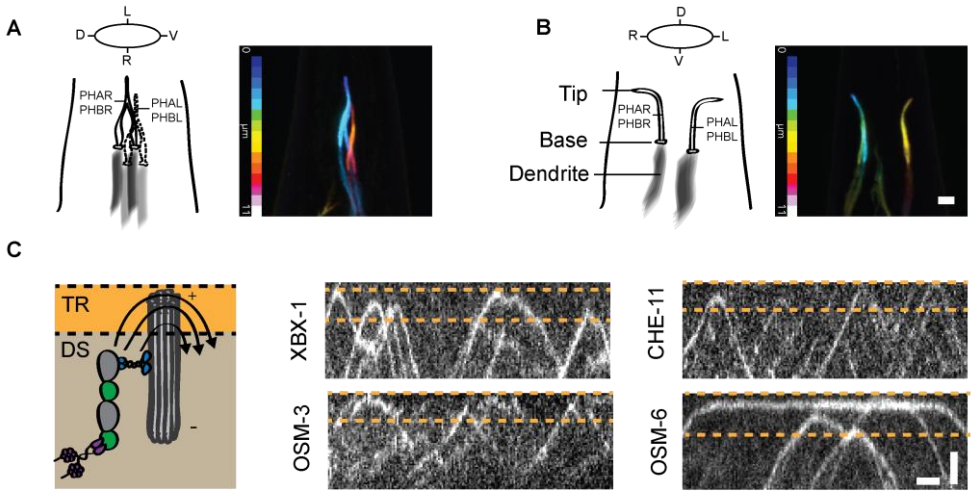

Figure 3.1: Single-molecule imaging reveals XBX-1, OSM-3, CHE-11 and OSM-6 turnarounds in a turnaround region at the ciliary tip.

A.–B. Sketch and corresponding 3-dimensional confocal microscopy images of different-plane (**A**, ciliary tip out of focus) and same-plane (**B**, ciliary tip in focus) orientation of chemosensory phasmid cilia in the *C. elegans* tail using TBB-4::EGFP. Scale bar: 1 µm; colors indicate depth. D, dorsal; V, ventral; L, left; R, right. **C.** Left: cartoon of the tip turnaround region (TR) of the ciliary distal segment (DS). Light grey: microtubules (+ and – indicate plus-ends and minus-ends); green and dark grey: IFT particles; blue: OSM-3; purple: dynein. Right: Dotted lines on kymographs of XBX-1::EGFP (IFT dynein), OSM-3::paGFP, CHE-11::mCherry (IFT-A) and OSM-6::EGFP (IFT-B), obtained from single-molecule wide-field epifluorescence recordings, mark the TR. Vertical: distance, scale bar 1 µm. Horizontal: time, scale bar 2 s.

To visualize the dynamics of the IFT machinery at the ciliary tip, we made use of *C. elegans* strains generated with MosSCI single-copy genomic insertions, expressing fluorescently-tagged (i) CHE-11 (CHE-11::mCherry), as a marker for the IFT-particle sub-complex IFT-A [30], (ii) OSM-6 (OSM-6::EGFP) as a marker the IFT-particle sub-complex IFT-B [9, 31, 32], (iii) XBX-1 (XBX-1::paGFP and XBX-

1::EGFP) as a marker for IFT dynein [24, 26, 33, 34] and (iv) OSM-3 (OSM-3::paGFP and OSM-3::mCherry) [9, 35-37] (Supplementary Table 3.1). Using laser-illuminated wide-field epifluorescence microscopy [9, 24, 38], we generated image sequences with single-molecule sensitivity. From these sequences we first generated kymographs using *KymographClear* [39], allowing representation of multiple single-molecule trajectories in a static image. Kymographs like these clearly show that all four IFT components investigated reverse direction from anterograde to retrograde at the ciliary tip (Figure 3.1C). Surprisingly, all kymographs show that turnarounds do not occur at a single spot, but in a 0.5 - 1 μm region close to the tip (Figure 3.1C, Supplementary Table 3.2). This region might reflect the local axonemal structure in *C. elegans* chemosensory cilia, where the distal segment consists of a bundle of nine microtubules, which are dynamic [10] and might differ and fluctuate in length. Transient accumulations of IFT-train components can sometimes be directly observed in the images (Supplementary Figure 3.3). In most cases, these accumulations appear to be located slightly beyond the turnaround region. These could be extracellular vesicles containing ciliary proteins being prepared for release from the tip [40, 41].

Further inspection of the kymographs suggested that turnarounds are remarkably heterogeneous: in some turnaround events the directional switch appears instantaneous, while in others it appears to involve a substantial pause. To get more quantitative insight in the turnaround behavior, we performed single-molecule tracking on the original image sequences, with a localization accuracy of ~40 nm [9, 42]. To obtain a coordinate system along and perpendicular to each cilium, a spline was drawn along the cilium (Figure 3.2A). Single-molecule localizations were then mapped on this local coordinate system, as described before [9]. Single-molecule trajectories further confirmed heterogeneous pausing behavior during turnarounds (Figure 3.2B, Supplementary Figure 3.2).

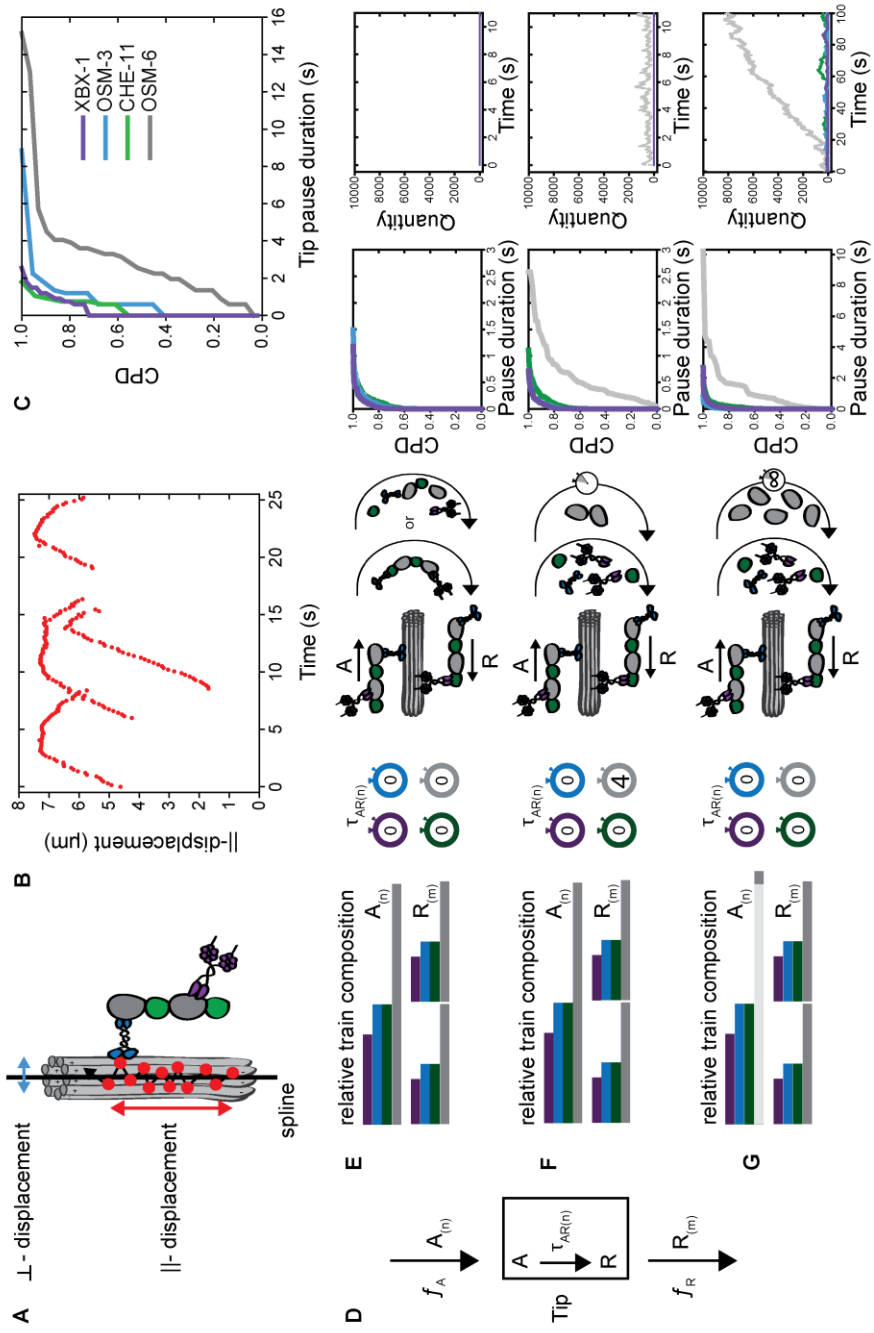
A
⊥- displacement
||- displacement
spline
B
||-displacement (µm)
Time (s)
C
CPD
Tip pause duration (s)
XBX-1
OSM-3
CHE-11
OSM-6
D
relative train composition
$A_{(n)}$
$R_{(m)}$
f_A
f_R
Tip
A
R
$\tau_{AR(n)}$
E
F
G
Quantity
Time (s)
Pause duration (s)
or

Figure 3.2 (left): OSM-6 dissociates from OSM-3, XBX-1 and CHE-11 at the ciliary tip.

A. Cartoon of the distal segment showing the parallel (∥, red) and perpendicular (⊥, blue) displacement of the IFT train along the ciliary spline. **B.** Example single-molecule trajectories of ∥-displacement (along the ciliary spline) at the ciliary tip. **C.** Cumulative probability distribution (CPD) of pause durations of XBX-1::EGFP (n=54, 13 worms), OSM-3::EGFP (n=22, 7 worms), CHE-11::EGFP (n=18, 5 worms) and OSM-6::EGFP (n=29, 5 worms) turnarounds. **D.** Schematic representation of the computer simulation of pause durations. Incoming anterograde trains of relative composition $A_{(n)}$ and frequency f_A are converted to retrograde trains of relative retrograde train composition $R_{(n)}$ and retrograde frequency f_R. The duration of the conversion process at the tip (box) is exponentially distributed with a time constant $\tau_{AR(n)}$ for each component. **E.-G.** Results of simulations for three distinct scenarios. **E.** $\tau_{AR(OSM\text{-}6)} = \tau_{AR(XBX\text{-}1)} = \tau_{AR(OSM\text{-}3)} = \tau_{AR(CHE\text{-}11)}$ **F.** $\tau_{AR(OSM\text{-}6)} >> \tau_{AR(XBX\text{-}1,\ OSM\text{-}3\ and\ CHE\text{-}11)}$ **G.** $A_{(OSM\text{-}6)} > R_{(OSM\text{-}6)}$ (more OSM-6 arrives at the cilia than is allowed to leave). For all three scenarios, from left to right: schematic representation of relative anterograde and retrograde train composition; anterograde to retrograde time constants $\tau_{AR(n)}$; cartoon depicting simulation results; CPD of pause durations in simulation results; and amount of each component at the tip as a function of time in simulation. Purple: XBX-1; blue: OSM-3; green: CHE-11; gray: OSM-6.

We next determined for each trajectory whether it involved a pause at the tip and if so, the duration of the pause. To this end, we calculated the displacement along the cilium between frames. A pause was scored when the average parallel displacement was less than 80 nm in 600 ms (4 frames). A cumulative probability distribution of the pause durations obtained using this algorithm (Figure 3.2C) reveals surprisingly distinct pause behavior between OSM-6 and the other IFT-train constituents. More than half of XBX-1, OSM-3 and CHE-11 molecules reverse direction without observable pause, while the rest pauses only relatively briefly (shorter than ~2 s). In contrast, almost all

OSM-6 molecules pause before turning around, including molecules that pause as long as 15 seconds. This significant difference in pause duration at turnaround between OSM-6 (median pause duration 2.5 s) and the other three IFT train components (median pause duration ≤600 ms) indicates that IFT-B dissociates from IFT dynein, OSM-3 and IFT-A at the tip. Our single-molecule findings are consistent with those reported for other organisms at the ensemble (IFT train) level, where IFT-B pausing has also been observed in *T. brucei* (~3.5 – 4 s) and *C. reinhardtii* (up to 2.5 s) [23, 43].

To further substantiate these experimental findings, we performed computer simulations of different turnaround scenarios (Figure 3.2D-G and Supplementary Table 3.3). We assumed a simple model (Figure 3.2D) in which anterograde trains with a given number of molecules A_n of IFT component n (motors or IFT particles) arrive at the tip with frequency f_A. Before departing as retrograde trains, components first need to convert from anterograde 'forms' of the components to retrograde. We model this as a stochastic process characterized by time constant $\tau_{AR(n)}$, which can be different for each component. After obeying specific departure requirements (e.g. containing a given, minimal amount of components; see below) trains can depart with composition $R_{(m)}$ and frequency f_R, which are output parameters of the simulation. Other output parameters are cumulative probability distributions of pause durations of individual IFT components and the amount of the components residing at the tip. In our simulations, we add a user-selectable amount of noise to the amount of motors in anterograde trains. First, we investigated a scenario where CHE-11, OSM-6, XBX-1 and OSM-3 convert from anterograde to retrograde with the same, short, time constant (Figure 3.2E and Supplementary Table 3.3 for all simulation parameters). As a specific retrograde departure requirement, we set a threshold (including noise) for minimum train size of half that of the anterograde trains (keeping the component ratios the same). This simulation yields comparable train compositions and frequencies with those observed in our previous experiments [9, 24]. As might be expected, in this simulation, pause distributions

are identical for the four components, at odds with our current experiments. In a second simulation, we kept τ_{AR} at the same low value for CHE-11, XBX-1 and OSM-3 while substantially increasing it for OSM-6. Train compositions and departure requirements were kept the same (Figure 3.2F). This simulation yields substantially longer pauses for OSM-6 than for the other components, quantitatively comparable to what we have observed in the experiments. In this simulation an initial accumulation of OSM-6, followed by a steady-state pool is observed at the tip. We failed to reproduce our experimental observations in ways other than assigning a larger time constant for anterograde-to-retrograde conversion (τ_{AR}) to OSM-6 than to the other components. As an example, we show a simulation with altered amounts and ratios of IFT components resulting in a net influx of OSM-6 at the tip (Figure 3.2G). Although this particular simulation reproduces the experimentally observed pausing behavior, it results in continuous accumulation of OSM-6 without reaching steady state, inconsistent with our experimental observations. Taken together, our single-molecule data and simulations indicate that OSM-6 behaves differently at the ciliary tip than the other components tested: while the other components are ready for incorporation in a retrograde train almost immediately after IFT-train disassembly, OSM-6 requires several seconds to convert from an anterograde to a retrograde moving state.

To further probe the nature of the single-molecule behavior of OSM-6 and other IFT-train components at the ciliary tip, we quantified their displacement perpendicular to the ciliary spline (Figure 3.2A). For each trajectory, we determined the maximum absolute displacement perpendicular to the cilium, during pauses and during anterograde or retrograde motion. We found that, on average, the range of perpendicular displacement is twice smaller for pausing than for moving molecules, suggesting that pausing molecules are spatially restricted at the ciliary tip (Figure 3.3A). This could be either due to specific interactions with microtubule plus ends or the ciliary membrane, or

due to ciliary narrowing in this region, as for example observed in EM images of *C. reinhardtii* flagella [44].

In a small subset of XBX-1 and OSM-3 trajectories that were not detected as pauses, we observed back-and-forth displacements along the cilium at the tip, prior to continuous retrograde movement towards the base (Figure 3.3C; OSM-3: n=5 out of 22 trajectories; XBX-1: n=8 out of 54 trajectories). In these trajectories, large displacements perpendicular to the cilium long axis can also be seen. It is possible that these particular trajectories are caused by opposite-polarity motors engaging in a tug-of-war, resulting in saltatory back-and-forth motion. Given the large displacement perpendicular to the cilium, it is, however, more likely that these trajectories belong to dissociated OSM-3 and XBX-1 motors exploring the ciliary space until they bind to an IFT particle. Whatever their exact origin, these trajectories do indicate that, in principle, there is enough space for single molecules to diffuse over substantial distances. Thus, the small perpendicular displacement of the IFT components (Figure 3.3D) is most likely caused by the interactions of these components with the microtubule tips or ciliary membrane. This is in line with the observation that IFT172 (an IFT-B subunit homologous to *C. elegans* OSM-1) interacts with EB1 at the microtubule plus-ends in *C. reinhardtii* flagella [45]. Such interactions could facilitate train reassembly, making turnarounds more efficient by preventing IFT components from diffusing away.

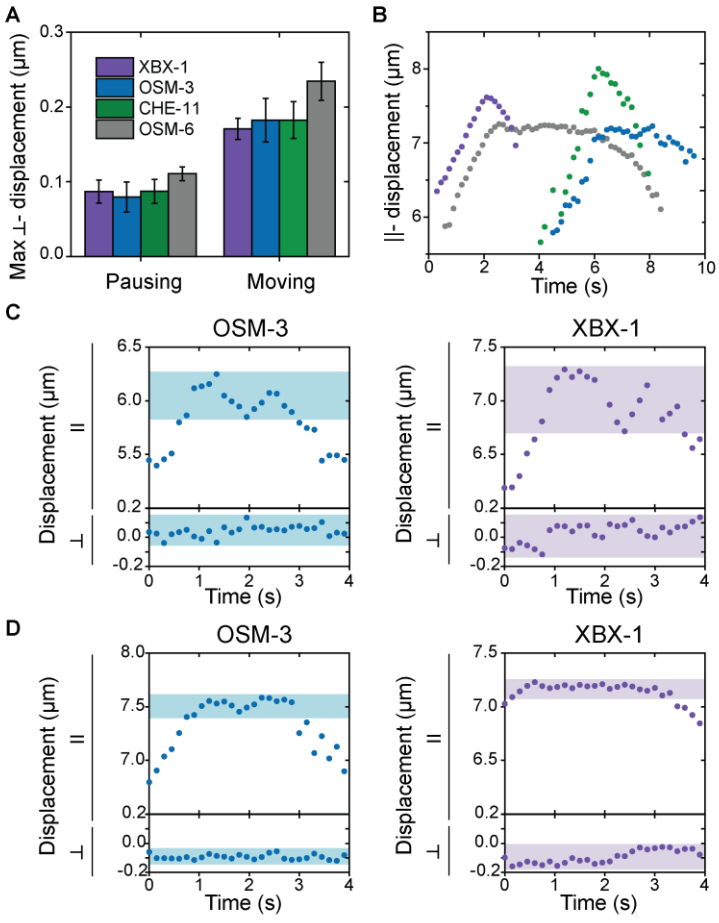

Figure 3.3: XBX-1 and OSM-3, but not CHE-11 and OSM-6, show spatially unconstrained pausing at the ciliary tip.

A. Average range of XBX-1::EGFP, OSM-3::EGFP, OSM-6::EGFP and CHE-11::EGFP ⊥-displacement (perpendicular to cilium spline). Error is SEM. **B.** Representative single-molecule trajectories of XBX-1::EGFP (purple), OSM-3::paGFP (blue), CHE-11::mCherry (green) and OSM-6::EGFP (grey) showing retrograde acceleration behavior after leaving the tip. **C.-D.** Representative single-molecule trajectories of displacement parallel (∥) and perpendicular (⊥) to the ciliary axis for OSM-3::EGFP (blue) and XBX-1::EGFP (purple) showing

spatially unconstrained (**C**) and constrained (**D**) displacement. The ∥-displacement range and ⊥-displacement range are shown.

Many turnaround trajectories involving a pause appeared symmetric, *i.e.* the velocities of anterograde arrival and retrograde departure are similar (Supplementary Figure 3.2E-H). In a substantial fraction of trajectories, however, the behavior is quite different: following turnaround, retrograde motion is initially very slow, followed by an abrupt acceleration to typical retrograde velocities (Figure 3.3B). Such behavior was observed for approximately half of the IFT-A (50%) and IFT-B (57%) trajectories involving a pause, while it was hardly observed for XBX-1 and OSM-3. We speculate that this acceleration behavior is caused by the sequential assembly of trains, with IFT-A and IFT-B initially forming the train backbone, followed by the docking of OSM-3 and IFT dynein. Incomplete trains contain few motors and, as a consequence, might start moving slowly. The subsequent docking of additional motors enables the trains to reach their maximum velocity.

In a final set of experiments, we probed whether turnaround behavior requires the specific axonemal structure of the distal segment: a bundle of nine microtubule singlets. To this end, we generated a *C. elegans* strain expressing fluorescently labeled XBX-1, but lacking OSM-3 function (Supplementary Table 3.1). It is well-established that *C. elegans* lacking OSM-3 cannot build the ciliary distal segment [46]. These cilia extend only up to the end of the proximal segment, with microtubules arranged in doublets (Figure 3.4A). Surprisingly, in the truncated cilia of these animals, XBX-1 shows well-defined single-molecule turnarounds (Figure 3.4B,C). Furthermore, pause durations are similar to those observed for animals expressing OSM-3 (Figures 3.4D and 3.2). These observations show that IFT turnaround does not depend on axoneme length and can occur efficiently on both singlet and doublet microtubules. This could indicate that the turnaround of IFT trains is triggered by reaching the end of the microtubule track.

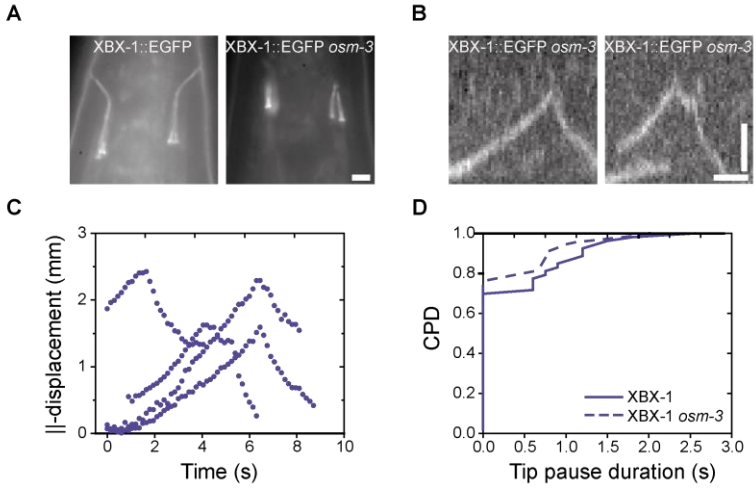

Figure 3.4: XBX-1 tip turnarounds in truncated cilia.

A. Representative summed fluorescence images of XBX-1::EGFP in wildtype (left) and *osm*-3 (right) *C. elegans*. Scale bar 2 µm. **B.** Representative kymographs of XBX-1::EGFP tip turns in *osm*-3 worms. Horizontal: time, scale bar 2 s. Vertical: distance, scale bar 1µm. **C.** Example single-molecule XBX-1::EGFP trajectories of ||-displacement at the ciliary tip in *osm*-3 animals. **D.** CPD plot of XBX-1::EGFP pause durations in *osm*-3 animals (dotted line, n=21 trajectories, 11 worms) and wildtype for comparison (solid line, Figure 3.2B, n=54 trajectories, 13 worms).

3.3 Discussion and conclusion

A key question in understanding bidirectional intracellular transport driven by opposite-polarity, microtubule-based motors is how cargo directionality is established. Here, we have studied the directional switch that occurs in IFT at the distal tips of *C. elegans* chemosensory cilia, where plus-end-directed, kinesin-2-driven IFT trains hand over transport to minus-end-directed IFT-dynein motors.

Experiments in different model organisms using genetics and co-immunoprecipitation methods have shaped our current understanding of the protein composition of IFT trains. During anterograde transport, the dynein light intermediate chain and, in *C. elegans*, OSM-3 have been shown to bind IFT-B [25, 26]. IFT dynein, however, has also been shown to bind to IFT-A, independently of IFT-B, in *Chlamydomonas*. Furthermore, *C. elegans* xbx-1 mutants are phenotypically similar to IFT-A mutants, suggesting that IFT dynein switches from IFT-B to IFT-A during tip turnaround [25, 26]. This model is consistent with the single-molecule trajectories we obtained, which show that single IFT-B molecules pause extensively at the tip whereas other IFT-train components do not. These findings indicate that the entire IFT-train machinery disassembles at the tip, and then reassembles for retrograde transport. This reassembly of the trains might be needed for IFT-dynein activation from cargo on anterograde trains to active driver of retrograde trains. Our data provides indications that the trigger for train disassembly, reassembly and turnaround is the trains arriving at the microtubule plus ends. Further investigations will be required to identify whether the turnaround cue is the actual 'derailing' of the trains (the trains running off the microtubule), or due to specific properties of the microtubule plus ends, such as +TIPs [47] or regional tubulin posttranslational modifications [48-50]. Proteins such as the BBSome are also likely to play a role in the regulation of IFT tip turnaround [51].

The turnaround of whole IFT trains was recently described in *Chlamydomonas* using the FRAP-based assay PhotoGate [29]. In this study, IFT trains were shown to split apart at the flagellar tip, with kinesin-II and IFT dynein returning to the base independently of one another: kinesin-II by diffusion and IFT dynein by active transport [29]. Contrary to *Chlamydomonas*, kinesin-II in *C. elegans* is localized to the proximal segment only and returns to the base by active, dynein-mediated transport instead of diffusion [9, 15, 24]. The kinesin-2 motor present at the *C. elegans* ciliary tip, OSM-3, turns and is actively transported back without substantial diffusion or pausing. Despite these inter-species differences, our findings reveal that key features of tip turnaround are

conserved. Notably, in both *Chlamydomonas* [29] and metazoan cilia (this work) tip turnaround has been demonstrated to be a multi-step, at least partially stochastic process.

Although both IFT particle sub-complexes A and B are transported bidirectionally and can bind motors, evidence in literature suggests disparate roles for IFT-A and IFT-B. In *C. elegans* cilia, there are approximately twice more IFT-B than IFT-A proteins [9]. IFT-A mutants often result in partially truncated cilia with sometimes accumulation of IFT proteins at the tip, whereas the IFT-B mutant phenotype is more severe, leading to abolished ciliogenesis or severely stunted cilia [46, 52, 53]. In agreement with these studies, our findings suggest a distinct role for IFT-B component OSM-6 that, in contrast to the other IFT components investigated, substantially pauses at the tip. This pause might be caused by a relatively slow (conformational) change in IFT-B required for incorporation in a retrograde train. Our observation that OSM-6 is spatially constrained during pauses, might, on the other hand, indicate that IFT-B provides a stable docking station at the tip preventing motors from diffusing into the ciliary space. In support of this hypothesis, an IFT-B component (but no IFT-A components) was found to interact with microtubule plus-end protein EB1 in *C. reinhardtii* [45]. Furthermore, several IFT-B components have tubulin binding sites [54, 55], necessary for the transport of tubulin as IFT cargo in ciliogenesis and ciliary maintenance. These binding sites might also be involved in the confinement of IFT components in the tip turnaround region [56].

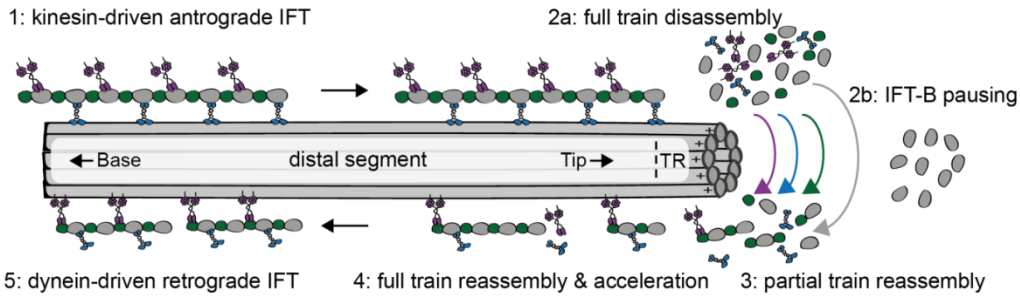

Figure 3.5: Schematic of tip turnaround events.

1. OSM-3-driven IFT trains drive IFT train transport over the distal segment toward the tip. 2. At the tip turnaround region (TR) of the distal segment, trains consisting of OSM-3, IFT dynein, IFT-A and IFT-B fully disassemble (a); IFT-B pauses, requiring several seconds before being ready for retrograde transport, while the other IFT components are immediately ready (b). 3. IFT trains containing few IFT-dynein motors depart at sub-maximum velocity 4. More IFT-dynein motors dock on the train, resulting in acceleration. 5. Dynein-driven IFT trains are transported back towards the ciliary base.

Taken together, our single-molecule data supports a turnaround model where IFT trains composed of IFT-A, IFT-B, IFT dynein and OSM-3 fully disassemble (Figure 3.5). Most IFT components do not diffuse into the ciliary space, but instead turn almost immediately (IFT-A, IFT dynein and OSM-3) or remain bound to the microtubule track or ciliary membrane during remodeling (IFT-B). When IFT dynein engages to initiate retrograde transport, incomplete trains can depart with lower velocity and accelerate once fully assembled.

3.4 Materials and methods

C. elegans strains

The *C. elegans* strains used in this study are listed in Supplementary Table 3.1. All strains were generated using the MosSCI single-copy genomic insertion method, as described previously [9, 57]. Nematode maintenance was performed using standard procedures.

Confocal fluorescence microscopy

Confocal fluorescence microscopy was employed to get insight into the 3-dimensional orientation of the phasmid cilia and the location of the ciliary tip. Young adult worms were immobilized using 5mM levamisole in M9 and mounted on 2% agarose pads in M9. Imaging was performed on a Nikon microscope based around a Ti-E inverted microscope body equipped with a A1R scan head, a LU4A laser module and GaAsP detectors. Depth-color-coded images were generated using ImageJ (http://imagej.nih.gov/ij).

Single-molecule fluorescence imaging and analysis

Young adult worms were immobilized using 5mM levamisole in M9 and mounted on 2% agarose pads in M9. Only worms oriented with the ciliary tip in focus were selected and imaged on a custom-built epi-illuminated wide-field microscope, as described before [38]. Strains were photobleached (EJP212, EJP76, EJP81 and EJP216) or photoactivated (EJP210, EJP32) to achieve single-molecule imaging conditions. Single-molecule kymographs were generated using the ImageJ (http://imagej.nih.gov/ij) plugin KymographClear (http://www.nat.vu.nl/~erwinp/downloads.html) [39]. Single-particle tracking was performed using custom-written MATLAB (MathWorks) routines using a linking algorithm [42], as described previously [9, 24]. A turnaround event was identified when a trajectory had a local maximum (position) along the axis parallel to the ciliary long axis and was preceded and followed by at least three

consecutive steps that did not qualify as a pause (see below). The turnaround region (Supplementary Table 3.2) was calculated by determining the range of turnaround locations (from the local maxima of each trajectory) per cilium in cilia where at least 3 tip turnaround trajectories were detected.

Pause determination

A MATLAB (MathWorks) routine was written to determine the occurrence and duration of tip pauses of trajectories of the four IFT components. To this end, we calculated the parallel displacement along the cilium between frames for 4 consecutive frames (150 ms per frame, 600 ms in total). A pause was scored when the average parallel displacement in 4 frames was less than 80 nm. To determine the duration of the pause, we shifted by one frame and calculated the parallel displacement along the next 4 frames until the average displacement exceeded 80 nm.

Simulations of tip residence time of IFT components

Custom-written simulations of tip turns were performed using LabVIEW (National Instruments). Groups (trains) of motors and particles arrived at the tip with a user-adjustable composition and frequency. Trains were subsequently allowed to depart from the tip again with user-selectable conditions. In addition, the composition and frequency of departing trains could be adjusted. An overview of the conditions used in this manuscript can be found in Supplementary Table 3. The simulation software can be found at: http://www.nat.vu.nl/~erwinp/downloads.html.

3.5 Acknowledgements

We thank B. Prevo for helpful discussions, D. Vorselen for help with the pausing algorithm and J.H. Broeke for help with confocal imaging. We acknowledge financial support from the Netherlands Organization for Scientific Research (NWO) via a VICI grant, an NWO-Groot grant and via a

Program Grant (“The Signal is the Noise”) of the Foundation for Fundamental Research on Matter (FOM).

3.6 Author contributions

Conceptualization and Methodology, J.M., J.v.K., F.O. and E.J.G.P.; Investigation and Formal Analysis, J.M. and J.v.K.; Resources, J.M., S.A. and E.J.G.P.; Writing – Original Draft, J.M. and E.J.G.P.; Writing – Review & Editing, J.M., J.v.K., F.O., S.A. and E.J.G.P; Funding Acquisition and Supervision, E.J.G.P.

3.7 References

1. Singla, V. & Reiter, J.F. The primary cilium as the cell's antenna: signaling at a sensory organelle. *Science (New York, N.Y.)* **313**, 629-633 (2006).
2. Scholey, J.M. Intraflagellar transport. *Annual review of cell and developmental biology* **19**, 423-443 (2003).
3. Rosenbaum, J.L. & Witman, G.B. Intraflagellar transport. *Nature reviews. Molecular cell biology* **3**, 813-825 (2002).
4. Song, L. & Dentler, W.L. Flagellar protein dynamics in Chlamydomonas. *The Journal of biological chemistry* **276**, 29754-29763 (2001).
5. Marshall, W.F. & Rosenbaum, J.L. Intraflagellar transport balances continuous turnover of outer doublet microtubules: implications for flagellar length control. *The Journal of cell biology* **155**, 405-414 (2001).
6. Iomini, C., Babaev-Khaimov, V., Sassaroli, M. & Piperno, G. Protein particles in Chlamydomonas flagella undergo a transport cycle consisting of four phases. *The Journal of cell biology* **153**, 13-24 (2001).
7. Bujakowska, K.M. *et al.* Mutations in IFT172 cause isolated retinal degeneration and Bardet-Biedl syndrome. *Human molecular genetics* **24**, 230-242 (2015).
8. Tobin, J.L. & Beales, P.L. The nonmotile ciliopathies. *Genetics in medicine : official journal of the American College of Medical Genetics* **11**, 386-402 (2009).
9. Prevo, B., Mangeol, P., Oswald, F., Scholey, J.M. & Peterman, E.J. Functional differentiation of cooperating kinesin-2 motors orchestrates cargo import and transport in C. elegans cilia. *Nature cell biology* **17**, 1536-1545 (2015).
10. Hao, L. *et al.* Intraflagellar transport delivers tubulin isotypes to sensory cilium middle and distal segments. *Nature cell biology* **13**, 790-798 (2011).
11. Bhogaraju, S., Engel, B.D. & Lorentzen, E. Intraflagellar transport complex structure and cargo interactions. *Cilia* **2**, 10 (2013).
12. Qin, H., Diener, D.R., Geimer, S., Cole, D.G. & Rosenbaum, J.L. Intraflagellar transport (IFT) cargo: IFT transports flagellar precursors to the tip and turnover products to the cell body. *The Journal of cell biology* **164**, 255-266 (2004).
13. Qin, H. *et al.* Intraflagellar transport is required for the vectorial movement of TRPV channels in the ciliary membrane. *Current biology : CB* **15**, 1695-1699 (2005).
14. Ye, F. *et al.* Single molecule imaging reveals a major role for diffusion in the exploration of ciliary space by signaling receptors. *eLife* **2**, e00654 (2013).
15. Snow, J.J. *et al.* Two anterograde intraflagellar transport motors cooperate to build sensory cilia on C. elegans neurons. *Nature cell biology* **6**, 1109-1113 (2004).
16. O'Hagan, R. & Barr, M.M. A motor relay on ciliary tracks. *Nature cell biology* **17**, 1517-1519 (2015).

17. Engel, B.D. *et al.* The role of retrograde intraflagellar transport in flagellar assembly, maintenance, and function. *The Journal of cell biology* **199**, 151-167 (2012).
18. Hou, Y. & Witman, G.B. Dynein and intraflagellar transport. *Experimental cell research* **334**, 26-34 (2015).
19. Pazour, G.J., Dickert, B.L. & Witman, G.B. The DHC1b (DHC2) isoform of cytoplasmic dynein is required for flagellar assembly. *The Journal of cell biology* **144**, 473-481 (1999).
20. Signor, D. *et al.* Role of a class DHC1b dynein in retrograde transport of IFT motors and IFT raft particles along cilia, but not dendrites, in chemosensory neurons of living Caenorhabditis elegans. *The Journal of cell biology* **147**, 519-530 (1999).
21. Vannuccini, E. *et al.* Two classes of short intraflagellar transport train with different 3D structures are present in Chlamydomonas flagella. *Journal of cell science* **129**, 2064-2074 (2016).
22. Stepanek, L. & Pigino, G. Microtubule doublets are double-track railways for intraflagellar transport trains. *Science (New York, N.Y.)* **352**, 721-724 (2016).
23. Buisson, J. *et al.* Intraflagellar transport proteins cycle between the flagellum and its base. *Journal of cell science* **126**, 327-338 (2013).
24. Mijalkovic, J., Prevo, B., Oswald, F., Mangeol, P. & Peterman, E.J. Ensemble and single-molecule dynamics of IFT dynein in Caenorhabditis elegans cilia. *Nature communications* **8**, 14591 (2017).
25. Pedersen, L.B., Geimer, S. & Rosenbaum, J.L. Dissecting the molecular mechanisms of intraflagellar transport in chlamydomonas. *Current biology : CB* **16**, 450-459 (2006).
26. Schafer, J.C., Haycraft, C.J., Thomas, J.H., Yoder, B.K. & Swoboda, P. XBX-1 encodes a dynein light intermediate chain required for retrograde intraflagellar transport and cilia assembly in Caenorhabditis elegans. *Molecular biology of the cell* **14**, 2057-2070 (2003).
27. Li, W., Yi, P. & Ou, G. Somatic CRISPR-Cas9-induced mutations reveal roles of embryonically essential dynein chains in Caenorhabditis elegans cilia. *The Journal of cell biology* **208**, 683-692 (2015).
28. Reck, J. *et al.* The role of the dynein light intermediate chain in retrograde IFT and flagellar function in Chlamydomonas. *Molecular biology of the cell* **27**, 2404-2422 (2016).
29. Chien, A. *et al.* Dynamics of the IFT machinery at the ciliary tip. *eLife* **6** (2017).
30. Behal, R.H. *et al.* Subunit interactions and organization of the Chlamydomonas reinhardtii intraflagellar transport complex A proteins. *The Journal of biological chemistry* **287**, 11689-11703 (2012).
31. Lucker, B.F. *et al.* Characterization of the intraflagellar transport complex B core: direct interaction of the IFT81 and IFT74/72 subunits. *The Journal of biological chemistry* **280**, 27688-27696 (2005).
32. Taschner, M., Kotsis, F., Braeuer, P., Kuehn, E.W. & Lorentzen, E. Crystal structures of IFT70/52 and IFT52/46 provide insight into intraflagellar

transport B core complex assembly. *The Journal of cell biology* **207**, 269-282 (2014).
33. Perrone, C.A. *et al.* A novel dynein light intermediate chain colocalizes with the retrograde motor for intraflagellar transport at sites of axoneme assembly in chlamydomonas and Mammalian cells. *Molecular biology of the cell* **14**, 2041-2056 (2003).
34. Grissom, P.M., Vaisberg, E.A. & McIntosh, J.R. Identification of a novel light intermediate chain (D2LIC) for mammalian cytoplasmic dynein 2. *Molecular biology of the cell* **13**, 817-829 (2002).
35. Ou, G., Blacque, O.E., Snow, J.J., Leroux, M.R. & Scholey, J.M. Functional coordination of intraflagellar transport motors. *Nature* **436**, 583-587 (2005).
36. Cole, D.G. *et al.* Chlamydomonas kinesin-II-dependent intraflagellar transport (IFT): IFT particles contain proteins required for ciliary assembly in Caenorhabditis elegans sensory neurons. *The Journal of cell biology* **141**, 993-1008 (1998).
37. Signor, D., Wedaman, K.P., Rose, L.S. & Scholey, J.M. Two heteromeric kinesin complexes in chemosensory neurons and sensory cilia of Caenorhabditis elegans. *Molecular biology of the cell* **10**, 345-360 (1999).
38. van Krugten, J. & Peterman, E.J.G. Single-Molecule Fluorescence Microscopy in Living Caenorhabditis elegans. *Methods in molecular biology (Clifton, N.J.)* **1665**, 145-154 (2018).
39. Mangeol, P., Prevo, B. & Peterman, E.J. KymographClear and KymographDirect: two tools for the automated quantitative analysis of molecular and cellular dynamics using kymographs. *Molecular biology of the cell* (2016).
40. Wang, J. *et al.* C. elegans ciliated sensory neurons release extracellular vesicles that function in animal communication. *Current biology : CB* **24**, 519-525 (2014).
41. Delling, M., DeCaen, P.G., Doerner, J.F., Febvay, S. & Clapham, D.E. Primary cilia are specialized calcium signalling organelles. *Nature* **504**, 311-314 (2013).
42. Jaqaman, K. *et al.* Robust single-particle tracking in live-cell time-lapse sequences. *Nature methods* **5**, 695-702 (2008).
43. Qin, H., Wang, Z., Diener, D. & Rosenbaum, J. Intraflagellar transport protein 27 is a small G protein involved in cell-cycle control. *Current biology : CB* **17**, 193-202 (2007).
44. Doroquez, D.B., Berciu, C., Anderson, J.R., Sengupta, P. & Nicastro, D. A high-resolution morphological and ultrastructural map of anterior sensory cilia and glia in Caenorhabditis elegans. *eLife* **3**, e01948 (2014).
45. Pedersen, L.B. *et al.* Chlamydomonas IFT172 is encoded by FLA11, interacts with CrEB1, and regulates IFT at the flagellar tip. *Current biology : CB* **15**, 262-266 (2005).
46. Perkins, L.A., Hedgecock, E.M., Thomson, J.N. & Culotti, J.G. Mutant sensory cilia in the nematode Caenorhabditis elegans. *Developmental biology* **117**, 456-487 (1986).

47. Akhmanova, A. & Steinmetz, M.O. Microtubule +TIPs at a glance. *Journal of cell science* **123**, 3415-3419 (2010).
48. Redeker, V. *et al.* Mutations of tubulin glycylation sites reveal cross-talk between the C termini of alpha- and beta-tubulin and affect the ciliary matrix in Tetrahymena. *The Journal of biological chemistry* **280**, 596-606 (2005).
49. Wloga, D., Joachimiak, E., Louka, P. & Gaertig, J. Posttranslational Modifications of Tubulin and Cilia. *Cold Spring Harbor perspectives in biology* (2016).
50. Hammond, J.W., Cai, D. & Verhey, K.J. Tubulin modifications and their cellular functions. *Current opinion in cell biology* **20**, 71-76 (2008).
51. Wei, Q. *et al.* The BBSome controls IFT assembly and turnaround in cilia. *Nature cell biology* **14**, 950-957 (2012).
52. Pazour, G.J. *et al.* Chlamydomonas IFT88 and its mouse homologue, polycystic kidney disease gene tg737, are required for assembly of cilia and flagella. *The Journal of cell biology* **151**, 709-718 (2000).
53. Qin, H., Rosenbaum, J.L. & Barr, M.M. An autosomal recessive polycystic kidney disease gene homolog is involved in intraflagellar transport in C. elegans ciliated sensory neurons. *Current biology : CB* **11**, 457-461 (2001).
54. Taschner, M. *et al.* Intraflagellar transport proteins 172, 80, 57, 54, 38, and 20 form a stable tubulin-binding IFT-B2 complex. *The EMBO journal* **35**, 773-790 (2016).
55. Bhogaraju, S. *et al.* Molecular basis of tubulin transport within the cilium by IFT74 and IFT81. *Science (New York, N.Y.)* **341**, 1009-1012 (2013).
56. Taschner, M. & Lorentzen, E. The Intraflagellar Transport Machinery. *Cold Spring Harbor perspectives in biology* **8** (2016).
57. Frokjaer-Jensen, C. *et al.* Single-copy insertion of transgenes in Caenorhabditis elegans. *Nature genetics* **40**, 1375-1383 (2008).

3.8 Supplementary Figures

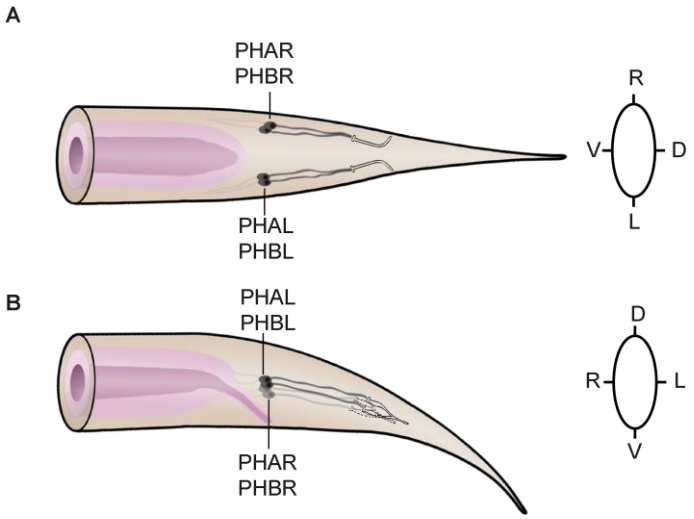

Supplementary Figure 3.1: Cartoon of cilium orientation for imaging tip dynamics.

3-Dimensional orientation of *C. elegans* PHA (PHAL and PHAR) and PHB (PHBL and PHBR) dendrites extending posteriorly from the cell bodies and terminating in phasmid cilia. Ciliary position relative to the rectal opening (pink) determines whether R and L phasmid cilia are in the same (**A**) or different (**B**) focal plane. D (dorsal), V (ventral), R (right), L (left).

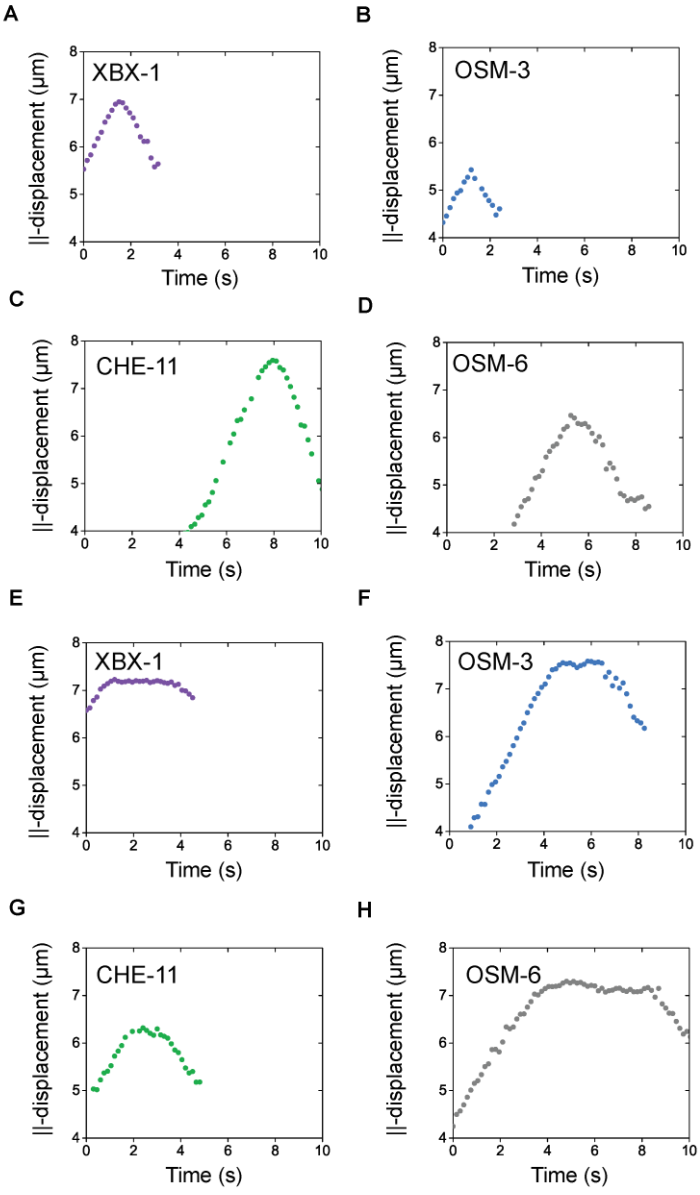

Supplementary Figure 3.2: Direct-turn and pausing single-molecule fluorescence trajectories.

Examples of direct-turn (**A-D**) and pausing (**E-H**) trajectories for XBX-1::EGFP, OSM-3::paGFP, CHE-11::mCherry and OSM-6::EGFP.

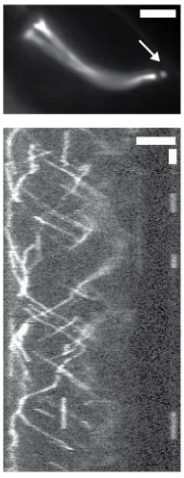

Supplementary Figure 3.3 (left): Secondary accumulation of OSM-6 at the ciliary tip.

Representative OSM-6::EGFP summed fluorescence image (top; scale bar 2 μm) and kymograph (bottom; horizontal: distance, scale bar 2 μm; vertical: time, 2 s).

3.9 Supplementary Tables

Strain	Genotype	Short notation
EJP210	*vuaSi210 [pJM10; Pxbx-1::xbx-1::paGFP; cb-unc-119(+)] I; xbx-1(ok279)* V	XBX-1::paGFP
EJP212	*vuaSi26 [pJM6; Pxbx-1::xbx-1::EGFP; cb-unc-119(+)] I; vuaSi2 [pBP22; Posm-3::osm-3::mCherry; cb-unc-119(+)] II; osm-3(p802)* IV; *xbx-1(ok279)* V	XBX-1::EGFP and OSM-3::mCherry
EJP32	*vuaSi8 [pBP31; Posm-3::osm-3::paGFP; cb-unc-119(+)] II; osm-3(p802)* IV	OSM-3::paGFP
EJP76	*vuaSi15 [pBP36; Posm-6::osm-6::eGFP; cb-unc-119(+)] I; unc-119(ed3)* III; *osm-6(p811)* V	OSM-6::EGFP
EJP81	*vuaSi24 [pBP43; Pche-11::che-11::mCherry; cb-unc-119(+)] II; unc-119(ed3)* III; *che-11(tm3433)* V	CHE-11::mCherry
EJP216	*vuaSi216 [pJM6; Pxbx-1::xbx-1::EGFP; cb-unc-119(+)] I; osm-3(p802)* IV; *xbx-1(ok279)* V	XBX-1::paGFP *osm-3*
EJP401	*vuaSi401 [pSA401; Ptbb-4::tbb-4::eGFP;cb-unc-119(+)]I*	TBB-4::EGFP

Supplementary Table 3.1: Strains used in this study.

Particle	Length tip turnaround region (µm)
XBX-1::eGFP XBX-1::paGFP	1.03 ± 0.27
OSM-3::paGFP OSM-3::mCherry	0.68 ± 0.28
CHE-11::mCherry	0.75 ± 0.17
OSM-6:eGFP	0.56 ± 0.22

Supplementary Table 3.2: Length tip turnaround region.
The tip turnaround region for XBX-1 (n = 42 trajectories), OSM-3 (n = 14), CHE-11 (n = 16) and OSM-6 (n = 25). Error shows SEM.

scenario / input	Figure 3.2E		Figure 3.2F		Figure 3.2G	
Time points	100000		100000		100000	
Trains in(/time)	0.01		0.01		0.01	
Noise (SD/Mean)	0.2		0.2		0.2	
#IFT-A/Train in	100		100		100	
#IFT-B/Train in	200		200		210	
#OSM-2/Train in	100		100		100	
#Dynein/Train in	75		75		75	
$\tau_{AR\ IFT\text{-}A}$ (/Time)	100		100		100	
$\tau_{AR\ IFT\text{-}B}$ (/Time)	100		0.004		100	
$\tau_{AR\ OSM\text{-}3}$ (/Time)	100		100		100	
$\tau_{AR\ Dynein}$ (/Time)	100		100		100	
Tip departure condition	Given size + noise leaves; rest stays		Given size + noise leaves; rest stays		User selectable output train size, rest leaves	
Input tip departure condition	#IFT-A/Train out, rest is proportional	50	#IFT-A/Train out, rest is proportional	50	#IFT-A / Train out	50
					#IFT-B / Train out	100
	Noise (SD/Mean) out	0.2	Noise (SD/Mean) out	0.2	#OSM-3 / Train out	50
					#Dynein / Train out	38

Supplementary Table 3.3: Parameter table for tip turnaround simulations in Figure 3.2 D-G.